Formation mechanism of bound states in graphene point contacts

Hai-Yao Deng,[1] Katsunori Wakabayashi,[1,*] and Chi-Hang Lam[2,†]

[1]*International Center for Materials Nanoarchitechtonics, National Institute for Materials Science, Namiki 1-1, Tsukuba 305-0044, Japan*
[2]*Department of Applied Physics, Hong Kong Polytechnic University, Hung Hom, Hong Kong*

Electronic localization in narrow graphene constrictions is theoretically studied, and it is found that long-lived ($\sim$1 ns) quasibound states (QBSs) can exist in a class of ultrashort graphene quantum point contacts (QPCs). These QBSs are shown to originate from the dispersionless edge states that are characteristic of the electronic structure of generically terminated graphene, in which pseudo-time-reversal symmetry is broken. The QBSs can be regarded as interface states confined between two graphene samples, and their properties can be modified by changing the sizes of the QPC and the interface geometry. In the presence of bearded sites, these QBSs can be converted into bound states. Experimental consequences and potential applications are discussed.

PACS number(s): 73.22.Pr, 72.80.Vp, 73.40.−c

I. INTRODUCTION

Quantum point contacts (QPCs), which are narrow constrictions connecting two wider samples, constitute fundamental building blocks of miniaturized devices such as quantum dots and qubits [1,2]. Being open systems, QPCs are usually incapable of supporting atomistically small quasibound states (QBSs) [3,4]. However, if they exist, QBSs can radically affect the properties of a system. For example, they might trap electrons and produce local magnetic moments [5–12], which can cause spin-dependent transport through a QPC.

Graphene, which is a one-atom-thick carbon sheet, has attracted tremendous attention in the past decade owing to its novel physical properties and potential applications for future electronic devices [13,14]. Nanostructures made of graphene can be patterned using the lithography technique [15]. Graphene QPCs have been fabricated and extensively studied [16–23]. A shortest-possible QPC, which is made of a single hexagon and makes an aperture for electrons, has been theoretically examined [22], and typical wave diffraction patterns were predicted. To date, all graphene QPCs investigated have been designed to connect the middle of samples, as sketched in Fig. 1(a), and no signatures of electron localization were found in the ballistic limit.

In this paper, we systematically study a different type of graphene QPC, where two graphene samples are connected near the edges as shown in Fig. 1(b). In these QPCs, the edge states, which appear on zigzag-shaped graphene edges at zero energy [24–26], are shown to dominate the electronic transport properties. For a half-graphene plane with a perfect zigzag edge, the edge states are nonbonding and are located on only one of the two sublattices. It has been shown that the edge states are crucial in determining the magnetic and transport properties of nanostructured graphene systems [25,27–36].

In conventional graphene QPCs, the edge states have negligible effects because they are far from the QPC. However, we show that electrons can be localized in QPCs as depicted in Fig. 1(b), i.e., where edge states located on different sublattices are coupled, resulting in the formation of

QBSs. These QBSs can live up to $\tau_{\mathrm{QBS}} \sim 1$ ns for sufficiently large samples, and their wave functions can spread over only a few lattice constants. Their lifetimes can be tuned by changing the geometry of the QPC and the size of the sample, whereas their energies $\varepsilon_{\mathrm{QBS}}$ are found to be insensitive to sample dimensions. These QBS may be used as few-level quantum dots and artificial atoms.

We organize the paper as follows. In Sec. II, we classify the edge-connected graphene QPCs into three classes and give a brief overview of the results. In Sec. III, we describe the formation mechanism of QBSs using the Green's-function approach. In Sec. IV, we apply the theory to an example QPC, where analytical results are obtained and compared to numerical calculations. Finally, in Sec. V, we discuss some experimental signatures and potential applications.

II. OVERVIEW

Figure 1(c) schematically shows the QPC that connects two graphene samples of the same width W near their edges. This QPC can be taken as an aperture for electron waves. The length and width of the QPC are L and W_c, respectively. Each graphene sample is geometrically confined by three edges, which are denoted by e_1, e_2, and $\bar{e}_2$ (e'_1, e'_2, and $\bar{e}'_2$) for the left-hand (right-hand) sample. We have assumed that e_2 (e'_2) is parallel with $\bar{e}_2$ ($\bar{e}'_2$). This condition is not necessary but facilitates the analysis. The interface edges (i.e., e_1 and e'_1) are assumed to be parallel for a smooth joint. Furthermore, we presume each edge to be either a perfect armchair (AC) or zigzag (ZZ) (i.e., the angles θ and θ' are integers of $\frac{\pi}{6}$). According to the edge structure, we can classify the QPCs into three classes of configurations as shown in Fig. 2. The details of each class are described below.

For class I, all edges in a QPC are AC, as shown in Fig. 2(a). Because there are no edge states in this class, the resulting QPCs resemble conventional QPCs and are therefore not further addressed in this paper.

For class II, the edges e_1 and e'_1 are ZZ, whereas the edges e_2 and e'_2 are AC. An example is given in Fig. 2(b). In this class, edge states appear on e_1 and e'_1. However, these edge states are no more than surface states, whose wave functions are bound to e_1 (e'_1); i.e., the wave function exponentially decays away from the QPC as schematically shown in Fig. 2(b).

---

*Corresponding author: wakabayashi.katsunori@nims.go.jp
†Corresponding author: c.h.lam@polyu.edu.hk

(a) Connecting near the middles

(b) Connecting near the edges
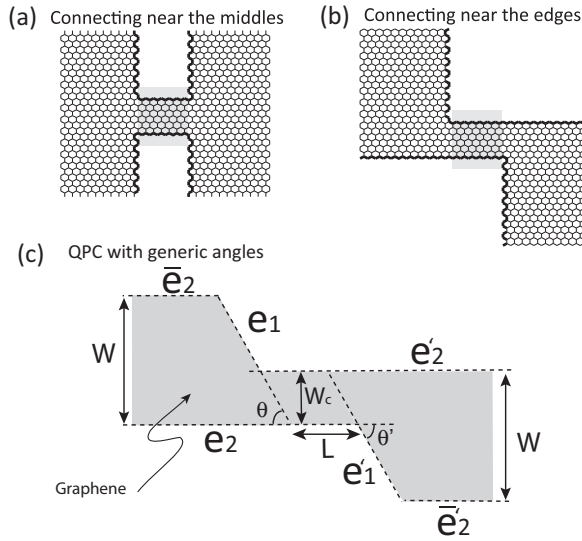
(c) QPC with generic angles

FIG. 1. (a) Schematic of the QPC connecting samples near the middle. (b) Schematic of the QPC connecting samples near the edge, where edge states can play an important role in electron transmission. (c) Schematic of the generic graphene QPCs connecting samples near the edge. Both samples infinitely extend along the edges e_2 and e'_2. The angles θ and θ' can be taken to be the same without loss of generality.

Because the edge states do not extend along e_2 (e'_2), they do not directly participate in electronic transport. Therefore, this class of QPCs simply admixes the surface states bound on e_1 with those on e'_1, yielding (quasi-) bound states.

For class III, our main interest lies in this third class. The interface edges e_1 and e'_1 can be either AC or ZZ, while the

edges e_2 and e'_2 (and hence $\bar{e}_2$ and $\bar{e}'_2$) are ZZ. There are two bunches of edge states located on different sublattices; these edge states extend along e_2 (e'_2) and $\bar{e}_2$ ($\bar{e}'_2$). In Fig. 2(c), we show an example of all ZZ edges. A different geometry is shown in Fig. 3, where the interface edges are AC.

The QBSs are formed because of the nonbonding nature of the edge states of the left and right samples (i.e., edges e_2 and e'_2). The QBS energy $\pm\varepsilon_{QBS}$ and lifetime τ_{QBS} are sensitive to the ratio W_c/W. QBSs have a long lifetime only for $W_c \ll \frac{W}{2}$. The quantity τ_{QBS} rapidly increases with W according to a power law; $\tau_{QBS} \sim (\frac{W}{W_0})^3$ ps, whereas ε_{QBS} is insensitive to W. Here W_0 is a length scale, which is around $86a \approx 21$ nm for $\theta = \theta' = \frac{\pi}{2}$. In general, QBS causes resonant scattering which leads to a resonance peak in the conductance g of the QPC. For large W, g takes on a symmetric Breit-Wigner form:

$$g \approx g_m \frac{\Gamma_{QBS}^2}{(\varepsilon_F - \varepsilon_{QBS})^2 + \Gamma_{QBS}^2}, \tag{1}$$

where $g_m \sim 1$ in units of $g_0 = \frac{2e^2}{h}$, ε_F is the Fermi level, and $\Gamma_{QBS} = \frac{\hbar}{\tau_{QBS}}$ denotes the level-broadening parameter. For finite W, the background contribution leads to an asymmetric line shape for g, i.e., Fano resonances [37].

III. THEORY: T-MATRIX FORMALISM

A. Model

In this section, we analyze the electronic properties of graphene QPCs using transition-matrix (T-matrix) formalism based on the nearest-neighbor tight-binding model [38]. We refer to the geometry shown in Fig. 2(c) for clarity. The enlarged view of the QPC is displayed in Fig. 2(d), where
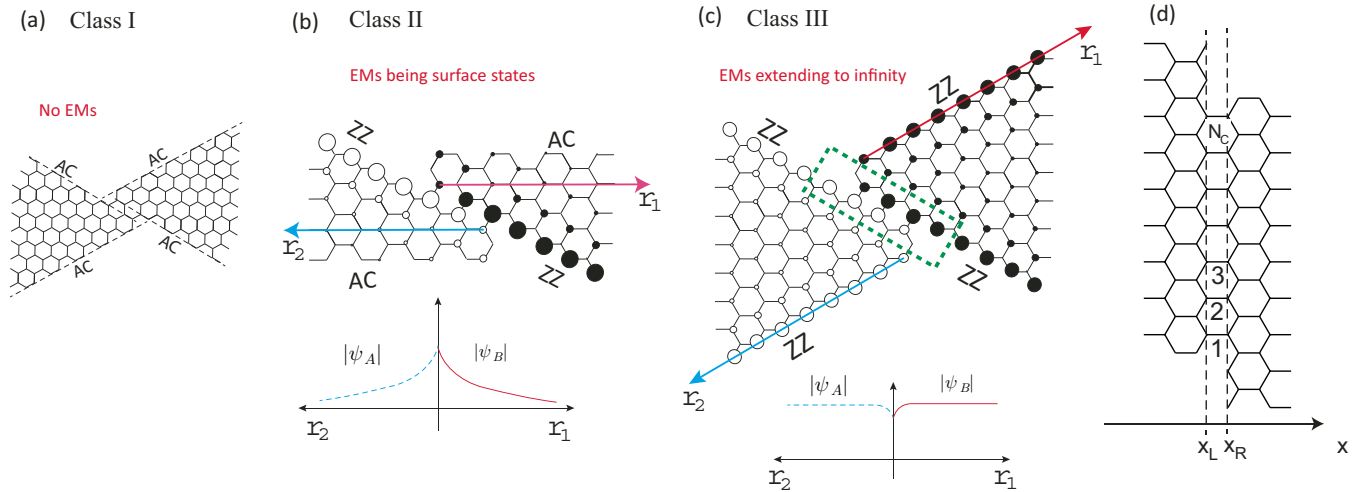

FIG. 2. (Color online) Classification of QPCs connecting samples near the edges. (a) Example of class I, which has all AC edges and no edge state. QPCs in this class are similar to QPCs connecting near the middle of samples. (b) Example of class II, for which the interface edges are ZZ but the extending edges are AC. In this class the edge states exponentially decay from the interface and are localized near the interfaces, i.e., bound states. Here the white (black) circles indicate the charge density of edge states on the A (B) sublattice sites. The schematic charge densities of the edge state are for isolated samples [41]. (c) Example of class III, for which the extending edges are ZZ, whereas the interfacing edges can be either ZZ (as in the example shown here) or AC (as in the example shown in Fig. 3). In this class, edge states also exist. However, they are not bound states as indicated by the schematic wave functions of semi-infinite isolated samples (bottom panel). Nevertheless, bound states emerge when QPCs are present. (d) Enlarged view of QPC [indicated by the dashed rectangle in panel (c)]. The QPC contains N_c connecting bonds.
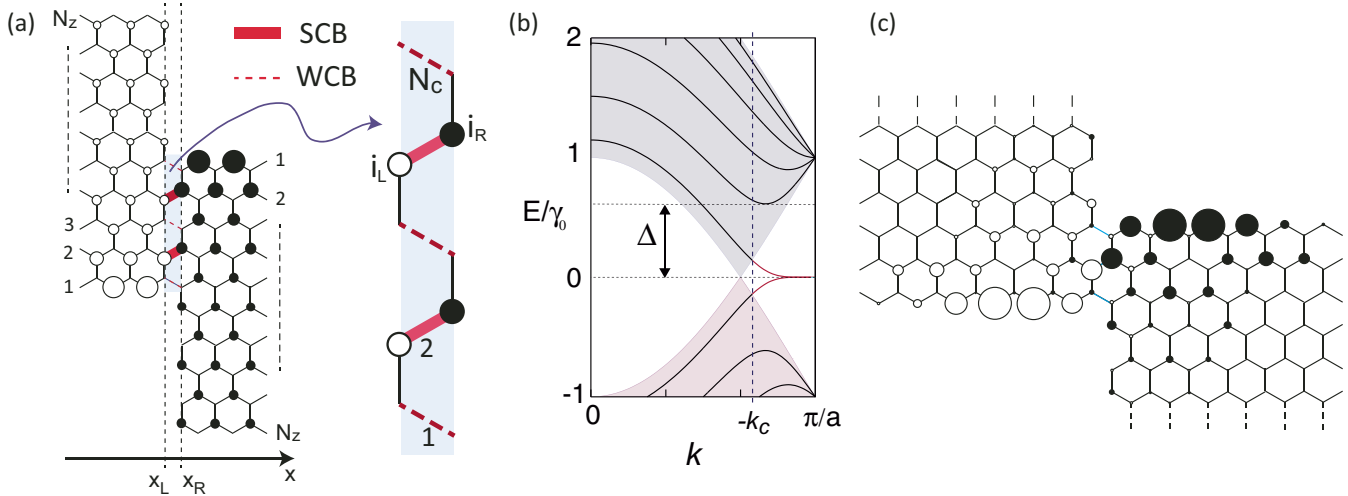
FIG. 3. (Color online) (a) Class-III QPC with rectangular corners with $N_c = 5$ connecting bonds. In this QPC, the edge states have amplitude on sublattice A (indicated by the white circle) for the left-hand graphene sample, whereas they have amplitude on sublattice B (indicated by the black circle) for the right-hand graphene sample. The SCBs and WCBs alternate with each other. (b) Energy spectrum for a semi-infinite ribbon consisting of $N_z = 6$ zigzag chains. Shaded areas indicate the spectrum of bulk graphene. Edge states appear in $k_c < k \leqslant \pi/a$ (red segments). The black lines indicate the extended states. (c) Magnitude of the QBS wave function $\langle j|\text{QBS}\rangle$ in the vicinity of a SCB assuming a symmetric boundary condition, which can be observed in STM. The calculation was done for $N_z = 50$ and $\varepsilon_{\text{QBS}} \approx 0.04$.

the two graphene samples are connected via N_c connecting bonds. Each bond has a left- and right-hand end lying on $x = x_L$ and x_R, respectively. The end sites on $x = x_L$ (x_R) are labeled i_L (i_R), where the index i_L (i_R) runs over $1, 2, \ldots, N_c$. The graphene edge along $x = x_L$ (x_R) corresponds to edge e_1 (e_1') in Fig. 1(c).

The total Hamiltonian of the system can be written as $H = H_L + H_R + V$, where H_L (H_R) describes the left (right) isolated graphene sample while V stands for the QPC. Explicitly, we have

$$V = \sum_{i_L=1}^{N_c} \sum_{i_R=1}^{N_c} \gamma_{i_L,i_R}(|i_L\rangle\langle i_R| + \text{H.c.}), \quad (2)$$

where $\gamma_{i_L,i_R} = -\gamma_0 \delta_{i_L,i_R}$ with $\gamma_0 \approx 2.7$ eV and $\delta_{i,j}$ is Kronecker's function. We introduce the bare Green's function, $G_0(\varepsilon) = (\varepsilon + i0_+ - H_0)^{-1}$, with $H_0 = H_L + H_R$. For later use, we resolve the diagonal elements of G_0 as follows:

$$G_0^{i,i}(\varepsilon) = \sum_\mu |\psi_{i;\mu}|^2 (\varepsilon + i0_+ - \varepsilon_\mu)^{-1}, \quad \psi_{i;\mu} = \langle i|\mu\rangle, \quad (3)$$

where $|\mu\rangle$ are the eigenstates of H_0, i.e., $H_0|\mu\rangle = \varepsilon_\mu|\mu\rangle$. Now the T matrix can be defined as

$$T(\varepsilon) = (1 - VG_0)^{-1}V = V + VG_0V + (VG_0)^2V + \cdots, \quad (4)$$

where 0_+ denotes an infinitesimal positive number. In principle, this matrix captures all physical effects arising from scattering at the QPC. The QBS can be found by searching for the poles of $T(\varepsilon)$.

For further analysis, let us closely inspect the bonding character at the interface. We note that the N_c connecting bonds fall into two categories: strongly connecting bonds (SCBs) and weakly connecting bonds (WCBs). Introducing the bare local density of states (LDOS) on atomic site i at energy ε as $\rho_0(\varepsilon, i) = -\frac{1}{\pi} \text{Im}[G_0^{i,i}(\varepsilon)]$, a SCB is then defined to have

nonvanishing $\rho_0(0, i)$ on both $i = i_L$ and $i = i_R$, where i_L and $i_R = i_L$ denote the sites belonging to this bond. Similarly, a WCB is defined to lack this property. In the QPC shown in Fig. 2(c), all connecting bonds are SCBs. However, in the QPC shown in Fig. 3, which also belongs to class III, the SCBs and WCBs alternate with each other.

B. Energy and lifetime of QBS

In general, it is a formidable task to evaluate T exactly. Here we use two approximations. First, we neglect all interbond transitions (i.e., $T_{i_R,i_L} \propto \delta_{i_R,i_L}$). This is reasonable, because these transitions are higher-order processes in G_0 compared with intrabond transitions. Second, we assume $G_0^{i,i} \approx 0$ at low energies if i belongs to a WCB, which can be justified in the limit $\frac{W}{2} \gg W_c$. Then, we can easily derive that $T_{i_R,i_L}(\varepsilon) \approx -\gamma_0 \delta_{i_R,i_L}$ for WCBs and that

$$T_{i_R,i_L}(\varepsilon) \approx \frac{-\gamma_0 \delta_{i_R,i_L}}{1 - \gamma_0^2 G_0^{i_L,i_L}(\varepsilon) G_0^{i_R,i_R}(\varepsilon)}, \quad (5)$$

for SCBs [39]. Basically, this expression describes the physical processes in which an electron travels back and forth between the sites i_L and i_R, in analogy with back-and-forth bounces experienced by an electron sandwiched between two potential barriers [4]. Note that such processes increase returning probability and are responsible for the formation of QBSs.

The energy and broadening of QBS can be determined by seeking the poles of Eq. (5). Rewriting $\gamma_0^2 G_0^{i_L,i_L}(\varepsilon) G_0^{i_R,i_R}(\varepsilon) = R^{i_L,i_R}(\varepsilon) + iI^{i_L,i_R}(\varepsilon)$, the poles $z_{\text{QBS}} = \varepsilon_{\text{QBS}} + i\Gamma_{\text{QBS}}$ can be obtained via

$$1 - R^{i_L,i_R}(z_{\text{QBS}}) - iI^{i_L,i_R}(z_{\text{QBS}}) \approx 0. \quad (6)$$

As will be shown later, in the large W limit, we have

$$G_0^{i_\tau,i_\tau} \approx \frac{1}{\varepsilon}B_\tau - \frac{i}{\gamma_0}C_\tau, \quad (7)$$

where $\tau = L$ or R. B_τ and C_τ are real values, which vary from bond to bond. Later, we will see that C_τ decreases to zero with increasing W following a power law whereas B_τ approaches a constant $B_{\tau,\infty}$. Upon substitution, we immediately find

$$
\begin{pmatrix} \varepsilon_{\mathrm{QBS}} \\ \Gamma_{\mathrm{QBS}} \end{pmatrix} \approx \frac{-\gamma_0}{2(1 + C_L C_R)} \\
\times \begin{pmatrix} \pm\sqrt{4 B_L B_R - (B_L C_R - B_R C_L)^2} \\ B_L C_R + C_L B_R \end{pmatrix}. \quad (8)
$$

From this it follows that (1) there is a pair of QBSs with each SCB, whose energies are symmetric about zero; (2) the energy of the QBS is not sensitive to the sample width, i.e., $\varepsilon_{\mathrm{QBS}} \approx \pm\gamma_0\sqrt{B_L B_R} \approx \pm\varepsilon_\infty = \pm\gamma_0\sqrt{B_{L,\infty} B_{R,\infty}}$; and (3) the QBS has a broadening, Γ_{QBS}, which shrinks rapidly with W, as explained below.

It proves useful to rewrite Eq. (5) as

$$
T_{i_L=l,i_R=l}(\varepsilon) = -\frac{\gamma_0 \varepsilon^2}{(\varepsilon - z_{\mathrm{QBS},l})(\varepsilon + z^*_{\mathrm{QBS},l})}, \quad (9)
$$

where we have used Eq. (7) and l indicates the lth SCB. The maximum of $|T_{i_L=l,i_R=l}(\varepsilon)|$ occurs when $\varepsilon = \varepsilon_{\mathrm{QBS},l}$, for which we have

$$
T_{i_L=l,i_R=l}(\varepsilon_{\mathrm{QBS},l}) = -i\gamma_0 \frac{\varepsilon_{\mathrm{QBS},l}}{2\Gamma_{\mathrm{QBS},l}} \gg T_{i_L \neq l, i_R \neq l}(\varepsilon_{\mathrm{QBS},l}). \quad (10)
$$

Evidently, the lth SCB predominates for $\varepsilon \sim \varepsilon_{\mathrm{QBS},l}$.

Now we establish Eq. (7). For this purpose, we decompose Eq. (3) into its real and imaginary parts:

$$
G_0^{i_\tau,i_\tau}(\varepsilon) = \sum_\mu{}' |\psi_{i_\tau;\mu}|^2 (\varepsilon - \varepsilon_\mu)^{-1} - i\pi\rho_0(\varepsilon, i_\tau), \quad (11)
$$

where i_τ belongs to a SCB, $\rho_0(\varepsilon, i_\tau) = \sum_\mu |\psi_{i_\tau;\mu}|^2 \delta(\varepsilon - \varepsilon_\mu)$ is the aforementioned LDOS on site i_τ, δ denotes the Dirac δ function, and the prime indicates the principal value of the sum (which can be turned into an integral). The μ denotes either an extended state or an edge state. In the sum, the contributions from the extended states are of the order W^{-3} [40] and can then be neglected for large W, whereas the contributions from the edge states are roughly independent of W. Therefore, considering that edge states have zero energies at large W, we arrive at the $G_0^{i,i}$ as given in Eq. (7), with the coefficients given by

$$
B_\tau = \sum_{\mu=\text{edge states}} |\psi_{i_\tau;\mu}|^2, \quad C_\tau = -\pi\gamma_0 \rho_0(\varepsilon_{\mathrm{QBS}}, i_\tau). \\ (12)
$$

From B_τ one determines $\varepsilon_{\mathrm{QBS}}$. The quantity C_τ is found by comparing Eqs. (7) and (11). Equations (5), (7), and (12) constitute the foundation of the present theory. They are applicable to all QPC configurations exemplified in Fig. 2 in the limit $\frac{W}{2} \gg W_c$. In the next section, we discuss prototypical examples.

In the limit $W \to \infty$, the edge states approach those of two isolated half-infinite graphene planes. Accordingly, the quantity B_τ tends to a constant $B_{\tau,\infty}$ given by Eq. (12) with the edge states of two half planes. Simultaneously, C_τ tends

to zero, since $\rho_0(\varepsilon_{\mathrm{QBS}}, i_\tau)$ comes from only extended states whose wave functions vanish on i_τ as $W/W_c \to \infty$.

C. Wave functions of QBS

To derive the QBS wave function, we shall consider the QBS associated with the lth SCB, for which $i_L = i_R = l$. In the conventional scattering theory [38], the state vector is given by $|\mathrm{QBS}, l\rangle = |\psi_0\rangle + G_0 T |\psi_0\rangle$, where $H_0|\psi_0\rangle = \varepsilon_{\mathrm{QBS},l}|\psi_0\rangle$. We have explicitly included the index l to indicate the QBS in question. To specify the QBS wave function, $\Psi_l(j) \equiv \langle j|\mathrm{QBS}, l\rangle$, where j denotes an arbitrary site in the entire system, we have to impose boundary conditions on $\langle j|\psi_0\rangle$. Two types of boundary conditions are considered here.

Type I assumes an open system and is appropriate for studying transport properties. The $\Psi_l(j)$ is supposed to describe an electron wave incident from the left-hand sample, tunneling through the QPC and partially transmitted to the right-hand sample. The $\langle j|\psi_0\rangle$ describes the superposition of the incident wave and the totally reflected wave. We then find

$$
\Psi_l(j) \approx \langle j|\psi_0\rangle \\
+ T_{i_L,i_L}(\varepsilon_{\mathrm{QBS},l}) G_0^{j,i_L}(\varepsilon_{\mathrm{QBS},l})\langle i_L|\psi_0\rangle \\
+ T_{i_R,i_L}(\varepsilon_{\mathrm{QBS},l}) G_0^{j,i_R}(\varepsilon_{\mathrm{QBS},l})\langle i_L|\psi_0\rangle, \quad (13)
$$

where $i_L = i_R = l$. The third term describes the transmitted wave. Note that we have kept only the lth bond, which is reasonable according to Eq. (10).

Type II assumes a closed system, in which no current flows from left to right. It is suitable for describing scanning tunneling microscopy (STM). We then find

$$
\Psi_l(j) \approx \langle j|\psi_0\rangle + T_{i_L,i_R}(\varepsilon_{\mathrm{QBS},l}) \\
\times \big[G_0^{j,i_L}(\varepsilon_{\mathrm{QBS},l})\langle i_R|\psi_0\rangle \\
+ G_0^{j,i_R}(\varepsilon_{\mathrm{QBS},l})\langle i_L|\psi_0\rangle \big], \quad (14)
$$

where $i_L = i_R = l$. We have neglected the terms headed by T_{i_L,i_L} and T_{i_R,i_R}, which are smaller than the retained terms [39]. An example of $\Psi_l(j)$ is mapped in Fig. 3(c), where we see that $\Psi_l(j)$ extends over only a few lattice constants in space.

IV. EXAMPLE: $\theta = \theta' = \frac{\pi}{2}$

Let us illustrate the above theory for the rectangular-corner configuration shown in Fig. 3. In this case, isolated graphene samples are semi-infinite ribbons. Their wave functions can be obtained from those for infinite ribbons, for which analytical solutions have been established [27]. Thus, the coefficients B_τ and C_τ can be analytically obtained. For convenience, we express the width W in terms of the number of total zigzag chains N_z as $W = \frac{a}{2\sqrt{3}}(3N_z - 2)$.

A. Calculation of $\varepsilon_{\mathrm{QBS}}$ and Γ_{QBS}

The goal is to find the coefficients B_τ and C_τ. For this purpose, we need $\psi_{i;\mu}$, the wave function of mode $|\mu\rangle$, which can be represented as a superposition of two counterpropagating waves related by time-reversal symmetry appropriate to an ideal zigzag graphene ribbon. They can be

easily constructed, so we simply quote the results here:

$$\begin{pmatrix} \psi_{i_L;\mu} \\ \psi_{i_R;\mu} \end{pmatrix} = \sqrt{\frac{2a}{L}} e^{ika} \sin\left(\frac{ka}{2}\right) \begin{pmatrix} -\Phi_\mu(i_L) \\ \Phi_\mu(i_R) \end{pmatrix}. \quad (15)$$

In Eq. (15), $k \in [0, \pi/a]$ and L denotes the circumference of a virtual zigzag graphene tube used to discretize the values of k. Φ is the transverse component of the wave function. Note that μ is shorthand for a composite index, (k, u, s), where $u = 1, \ldots, N_z$ counts the sub-bands and $s = \pm$ is the particle-hole label, as sketched in Fig. 3(b).

Specific to each sub-band, there is a quantum number p_u, which is real at any k for $u < N_z$ [27]. However, for $u = N_z$, p is real only if $k \in [0, k_c]$ and it can be written as $p = \pi + i\eta$ if $k \in (k_c, \frac{\pi}{a}]$. For this particular sub-band, in the large N_z limit, whereby $k_c = \frac{2\pi}{3a}$, it holds as a good approximation that $\varepsilon_s(k) \approx 0$ and [42]

$$\begin{pmatrix} \Phi_{k,s}(i_L) \\ \Phi_{k,s}(i_R) \end{pmatrix} \approx \sqrt{\frac{1 - g_k^2}{2}} \begin{pmatrix} g_k^{i_L - 1} \\ g_k^{N_c - i_R} \end{pmatrix} \quad (16)$$

for $k > \frac{2\pi}{3a}$. Here $g_k = 2\cos(ka/2)$. For $k < \frac{2\pi}{3a}$, in the same limit, we instead have $\varepsilon_s(k) \approx s(g_k - 1)$ and

$$\begin{pmatrix} \Phi_{k,s}(i_L) \\ \Phi_{k,s}(i_R) \end{pmatrix} \approx \sqrt{\frac{1}{N_z}} \begin{pmatrix} \sin(p i_L) \\ \sin[p(N_c + 1 - i_R)] \end{pmatrix}, \quad (17)$$

where $p \approx (1 - \frac{1}{N_z})\pi$ and we have dropped the subscript u for this sub-band. Note that, as shown in Fig. 3(b), this sub-band is the only one available within the energy window $[-\Delta, \Delta]$, where $\Delta \approx 4\gamma_0 \cos(\frac{N_z - 1}{2N_z - 1}\pi)$.

To evaluate C_τ, we may presume that the QBS lies inside the single-channel energy window (i.e., $\varepsilon_{\text{QBS}} \in [-\Delta, \Delta]$). Then, the only contribution to ρ_0, i.e., C_τ, comes from the $u = N_z$ sub-band with $k \in [0, \frac{2\pi}{3a}]$, because these are the only states available in that energy window. This assumption, whose validity can be examined by consistency check, implies that the QBS lifetime is essentially set by the dispersing segment of the lowest sub-band. By using Eqs. (15) and (17), we obtain

$$\begin{pmatrix} C_L \\ C_R \end{pmatrix} \approx A \frac{\pi^2}{N_z^3} \begin{pmatrix} i_L^2 \\ (N_c + 1 - i_R)^2 \end{pmatrix}, \quad (18)$$

with $\quad A = -\frac{2a}{L}\pi \sum_{0 \leq k < \frac{2\pi}{3a}} \sin^2(\frac{ka}{2}) \delta[\varepsilon_{\text{QBS}}^2 - (g_k - 1)^2]$. Transforming it into an integral, we find $A = -\frac{\sin(x_0)}{2|\varepsilon_{\text{QBS}}|}$, with $x_0 \in (0, \frac{\pi}{3})$ given by $|\varepsilon_{\text{QBS}}| = 2\cos(x_R) - 1$. The quadratic dependences on i_L and N_c are notable in Eq. (18), which explains why long-lived QBSs only form when N_c is small.

We proceed to estimate B_τ. At energies near zero the primary contributions stem from the edge states. Actually, since $p_u \approx \frac{u-1}{N_z}\pi$ for any extended state [Fig. 3(b)] of any sub-band in the large N_z limit, the total contributions from the low-energy sector, i.e., including those with $u \sim N_z$, are of the order $\sim N_z^{-1} \sum_{u \sim N_z} |\sin(\frac{u-1}{N_z}\pi)|^2 \approx N_z^{-3}$ [40]. Nonetheless, the contribution from the edge states is of order unity, as indicated in Eq. (16). Thus, when N_z is large, the edge states dominate. If we neglect the dispersion of these states, which is reasonable for large N_z, we immediately confirm Eq. (12).

TABLE I. Theoretically evaluated parameters for certain SCBs (N_c, i_L) (obviously $i_R = i_L$ for a given bond) in the configuration shown in Fig. 3. From Eqs. (8) and (19), we see that $\Gamma_{\text{QBS}} N_z^3$ (given in the last column) is independent of N_z. All energies are in units of γ_0.

(N_c, i_L)	$B_{L,\infty}$	$B_{R,\infty}$	ε_∞	$\|A\|$	$C_L N_z^3$	$C_R N_z^3$	$\Gamma_{\text{QBS}} N_z^3$
(2,2)	0.04	0.21	0.09	9.7	386.7	96.7	42.5
(3,2)	0.04	0.04	0.04	21.8	870	870	34.8
(4,2)	0.04	0.017	0.026	33.5	1338	3011	71.5
(4,4)	0.009	0.21	0.044	19.7	3149	196.8	331.6

Using Eqs. (15) and (16), we find

$$\lim_{N_z \to \infty} \begin{pmatrix} B_L \\ B_R \end{pmatrix} = \begin{pmatrix} B_{L,\infty} \\ B_{R,\infty} \end{pmatrix}$$

$$= \frac{2a}{L} \sum_{\frac{2\pi}{3a} < k < \frac{\pi}{a}} \sin^2(ka/2)(1 - g_k^2) \begin{pmatrix} g_k^{2(i_L - 1)} \\ g_k^{2(N_c - i_R)} \end{pmatrix}, \quad (19)$$

which quickly diminish as N_c or i_L increases.

Note that the maximum values of $B_{L,\infty}$ and $B_{R,\infty}$ occur at $(N_c = 2, i_L = i_R = 2)$, in which case one finds $B_{L,\infty} \approx 0.04$ and $B_{R,\infty} \approx 0.21$, leading to $\varepsilon_\infty \approx 0.09\gamma_0$. Therefore, for most ribbons of interest, we indeed have $\varepsilon_\infty \in [-\Delta, \Delta]$, which is consistent with our initial assumption [43]. Another case of special interest is $N_c = 3$, for which we find $B_{L,\infty} = B_{R,\infty} \approx 0.04$, yielding $\varepsilon_\infty \approx 0.04\gamma_0$. We then see that the ε_∞ depends strongly on N_c. The parameters for other interesting cases have also been calculated and are tabulated in Table I.

B. Spatial profile of QBS

To visualize the QBS in real space, we calculated the wave function of the QBS according to Eq. (14) for the symmetric boundary condition. We neglected the first term in these equations, so the spatial profile of the QBS is completely determined by G_0^{j,i_L} and G_0^{j,i_R}, which can be easily evaluated numerically using the resolution of Eq. (3). In Fig. 3(c), we show the results for the symmetric configuration ($N_c = 3, i_L = 2$). As expected, the amplitudes are concentrated about the SCB, spreading over a few lattice constants. This distribution can be observed in STM (see Sec. V). It is worth noting that the SCB resembles a molecular junction between the graphene samples.

C. Conductance

Ultranarrow QPCs usually strongly reflect incident electron waves, as would be anticipated from diffraction theory in the subwavelength regime [44]. However, such reflections can be suppressed due to resonant tunneling from QBSs. In what follows, we calculate the conductance g of the QPC shown in Fig. 3(a) and derive Eq. (1).

We focus on the single-channel regime, i.e., $\varepsilon \in (0, \Delta)$, where the modes can each be labeled by just a wave number. We use k and q to denote the wave numbers for the left- and right-hand samples, respectively. Following standard tunneling theory [45], we obtain the conductance at zero

temperature as

$$g = L^2 v_F^{-2} |\langle q = k_F | T | k = k_F \rangle|^2, \qquad (20)$$

where $v_F = (\frac{d\varepsilon_k}{dk})_{k=k_F} \approx -a\gamma_0 \sin(k_F a/2)$ and $k_F \in (0, \frac{2\pi}{3a})$ denote the Fermi velocity (in units of $\hbar = 1$) and Fermi wave

number, respectively. By using Eq. (5), we find

$$\langle q | T | k \rangle \approx -\gamma_0 \sum_{\text{WCB}} \psi^*_{i_R,q} \psi_{i_L,k} + \sum_{\text{SCB}} \psi^*_{i_R,q} \psi_{i_L,k} T_{i_R,i_L}.$$

Substituting this in Eq.(20), we find $g = g_w + g_s + g_{ws}$, where g_w (g_s) involves only WCBs (SCBs) whereas g_{ws} involves both SCBs and WCBs. Explicitly, we have

$$\begin{pmatrix} g_w \\ g_{ws} \\ g_s \end{pmatrix} = L^2 v_F^{-2} \begin{pmatrix} \gamma_0^2 \left| \sum_{l=\text{WCB}} \psi^*_{i_R=l;k_F} \psi_{i_L=l;k_F} \right|^2 \\ -\gamma_0 \sum_{l=\text{SCB}} \sum_{l'=\text{WCB}} \psi^*_{i_R=l',k_F} \psi_{i_L=l',k_F} \psi^*_{i_R=l,k_F} \psi_{i_L=l,k_F} T_{i_R=l,i_L=l}(\varepsilon_F) \\ \left| \sum_{l=\text{SCB}} \psi^*_{i_R=l;k_F} \psi_{i_L=l;k_F} T_{i_R=l,i_L=l}(\varepsilon_F) \right|^2 \end{pmatrix}. \qquad (21)$$

For ε_F near the energy of a QBS, these terms scale with N_z as follows:

$$g_w \sim N_z^{-6}, \quad g_{ws} \sim N_z^{-3}, \quad g_s \sim N_z^0, \qquad (22)$$

which can be shown on the basis of two observations. First, from Eqs. (15) and (17) it follows that $\psi_{i_\tau;k} \sim N_z^{-3/2}$ in the limit $N_c \ll \frac{N_z}{2}$. Second, from Eqs. (9) and (10) it follows that $T_{i_R=l,i_L=l} \sim -\gamma_0 N_z^3$ if $\varepsilon_{l,\text{QBS}} \sim \varepsilon_F$ or $T_{i_R=l,i_L=l} \approx -\gamma_0$ otherwise. From this, we see that in the large-N_z limit the dominant contribution to g_{ws} and g_s stems from the SCB whose energy is the closest to ε_F. Now the scaling becomes clear: in g_w, the wave functions contribute the N_z^{-6} factor; in g_{ws}, this factor is raised by N_z^3 due to the T-matrix element, which contributes a N_z^3 factor; in g_s, two T-matrix elements appear and contribute N_z^6, which exactly cancels the N_z^{-6} from the wave functions.

The above analysis shows that, for ε_F close to the energy of a QBS, the g_w and g_{ws} can be neglected for large N_z. Thus, we find

$$g \approx g_s = L^2 v_F^{-2} \left| \psi^*_{i_R=l;k_F} \psi_{i_L=l;k_F} T_{i_R=l,i_L=l}(\varepsilon_F) \right|^2, \qquad (23)$$

where ε_F is near $\varepsilon_{\text{QBS},l}$. By Eqs. (9) and (17), this expression can be reduced to Eq. (1), with

$$g_m = 4 \sin^2(k_l a/2) \left| \Phi^*_{k_F}(i_R = l) \Phi_{k_F}(i_L = l) \right|^2 \left(\frac{\varepsilon_{\text{QBS},l}}{\Gamma_{\text{QBS},l}} \right)^2$$
$$\sim N_z^0, \qquad (24)$$

where $k_l \approx \frac{2\pi}{3a}$ is given by $\varepsilon_{k_l} = \varepsilon_{\text{QBS},l} \sim 0$. With the parameters given in Table I, it is easy to see that $g_m \approx 1$. We emphasize that Eq. (1) gives a good description only when $N_c \ll \frac{N_z}{2}$. Otherwise, additional contributions from WCBs and overlaps between adjacent QBS make the g asymmetric and more similar to a Fano resonance.

D. Numerical calculations

To verify the above results, we have performed numerical calculations based on the Landauer formalism and mode-matching method. Details of the scheme will be presented elsewhere.

The calculated conductances for wide ribbons with $N_c = 2,3,4$ are presented as circles in Fig. 4. For $N_c = 2,3$, one resonance peak is observed in the entire single-channel

regime, as shown in Fig. 4(a). Such peaks are interpreted as consequences of QBS, whose energy and lifetime set the position and half width of the peaks. As seen in Fig. 4(a), the line shape of each peak can be well captured by Eq. (1), which is a Lorentzian (solid curves). For $N_c = 4$, as shown in Fig. 4(b), two peaks are observed. The lower-energy peak is very sharp, whereas the higher-energy peak is much broader. These peaks are identified with QBSs belonging to the two SCBs, ($N_c = 4, i_L = 2$) and ($N_c = 4, i_L = 4$). The line shape can be described by a superposition of two Lorentzians, as noted in Fig. 4(b).

In Fig. 5 we examine the N_z dependences of three quantities: g_m, ε_{QBS}, and Γ_{QBS} in Figs. 5(a)–5(c), respec-
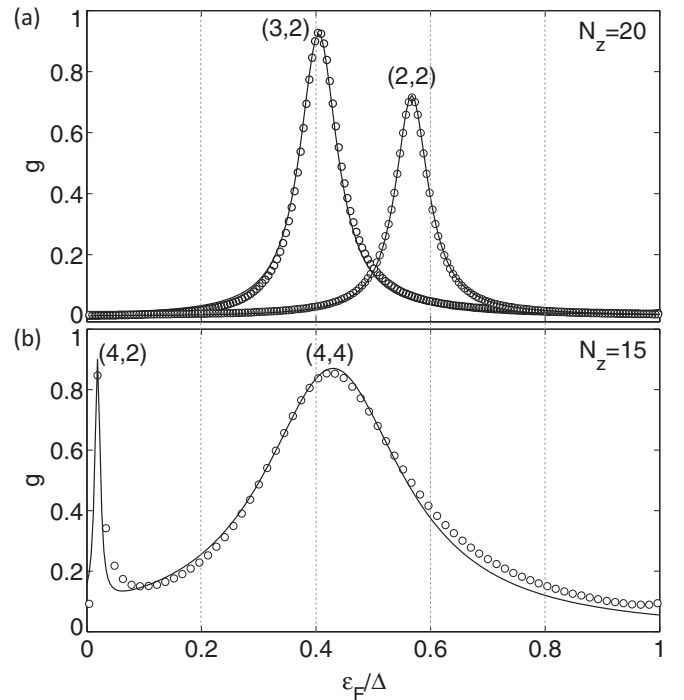

FIG. 4. Theory vs numerical calculations: energy dependence of conductance g for the QPC shown in Fig. 3. Circles represent numerical calculations while solid lines indicate fitting according to Eq. (1). The resonances are labeled (N_c, i_L), in the same manner as in Table I. In panel (a), only one SCB exists, whereas in panel (c) two SCBs exist. Each SCB leads to a peak in g.
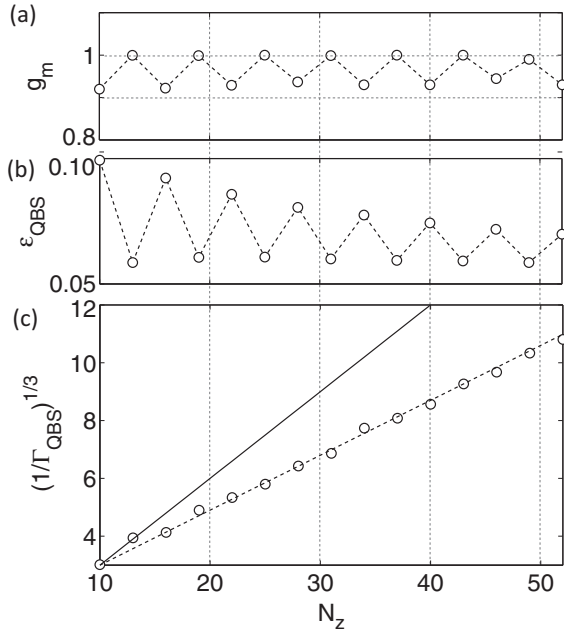
FIG. 5. Theory vs numerical calculations: N_z dependences of (a) peak conductance, (b) QBS energy, and (c) QBS broadening parameter (both in units of γ_0). The numerical calculations were done for the resonance (3,2) seen in Fig. 4(a). Our theory predicts roughly constant g_m, convergence of ε_{QBS} to ε_∞, and $\Gamma_{QBS} \sim N_z^{-3}$, all of which are consistent with numerical calculations. In panel (c), the solid curve has a slope of ~ 0.3 while the dashed curve has a slope of ~ 0.2. The dashed line is to guide the eye. The solid line shows results of theory, and circles show results of numerical calculations.

tively. According to the theory, we expect (1) the g_m to be roughly independent of N_z, (2) the ε_{QBS} to converge to ε_∞, and (3) the Γ_{QBS} to decrease as N_z^{-3}. All these features are borne out in numerical calculations, as evident in Figs. 5(a)–5(c). We notice a weak dependence of g_m and ε_{QBS} on the parity of N_z. This odd-even effect gradually disappears when N_z increases beyond ~ 250, which may be understood by observing that the edge state dispersion can be written as $\varepsilon_s(k) \approx 2s(-1)^{N_z+1}[1 + 2\cos(ka)]g_k^{N_z}$ in the large-N_z limit. The factor $(-1)^{N_z+1}$ may be the origin of such effects. For sufficiently large N_z ($N_z > \sim 250$), we have $\varepsilon_s(k) < \varepsilon_\infty$ for all $k \in (\frac{2\pi}{3a}, \frac{\pi}{a}]$. Equation (7) still holds, and we have $[B_L, B_R] \approx \frac{2a}{L}\sum_{k,s}\sin^2(\frac{ka}{2})(1 - g_k^2)(1 - \varepsilon_s(k)/\varepsilon_\infty)^{-1}[g_k^{2(i_L-1)}, g_k^{2(N_c-i_R)}]$, which does not display any parity effect. However, for N_z not that large ($N_z < \sim 250$), then ε_∞ will cut $\varepsilon_s(k)$ and parity effects can appear. Nonetheless, this case is not amenable to analytical expressions and will not be further discussed.

E. Role of bearded sites

Here we discuss the effect of bearded sites and show that they could lead to genuine bound states (i.e., vanishing Γ_{QBS}). For simplicity, we consider the rectangular-corner QPC with $N_c = 1$ (Fig. 6). In the absence of bearded sites, the connecting bond would be a WCB. However, bearded sites transform an edge state initially located on the A- (B-) sublattice to an edge state located on the B- (A-) sublattice [46], and they thus turn
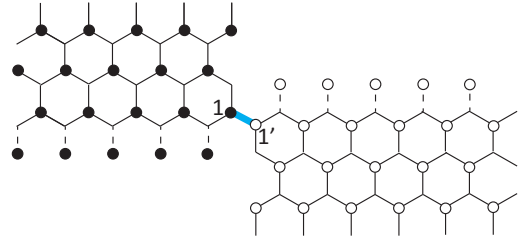

FIG. 6. (Color online) Bearded sites, represented by the circles attached to the dashed bonds, which turn a WCB into a SCB. A pair of real bound states form on the bond (see text). Geometrically, the SCB (blue bond) shown here is similar to the SCB ($N_c = 3, m = 2$) without bearded sites.

a WCB into a SCB. Then, one can show that $C_\tau = 0$ and then the level broadening vanishes, implying a pair of genuine bound states on this bond. Actually, bearded graphene is an insulator [46] with a real band gap separating the edge states from the extended states. Thus, the ρ_0 vanishes at the QBS energy, which is consistent with vanishing C_τ. The values of B_τ in the limit $N_z \to \infty$ are expected to be similar to those of the SCB ($N_c = 3, i_L = 2$) in the same limit without bearded sites, because the wave functions in both cases are the same [Eq. (17)].

V. DISCUSSIONS

An essential element in the QBS theory presented above relates to the existence of nonbonding edge states at zero energy. Generically, such states are originated from the breaking of pseudo-time-reversal symmetry, which is unique to the graphene lattice. Note that a perfect zigzag edge is not necessary for them to appear. Indeed, they could show up in graphene edges of almost any shape except for the perfect armchair one (in which case the symmetry is respected), even in the presence of a moderate external magnetic field [47]. The observation makes our theory more widely applicable.

Because the QBS extends over only a few lattice constants, the Coulomb repulsion might be relatively strong. Assuming an on-site repulsion of 10 eV [48], the repulsion between two electrons in QBS can be as large as 0.1 eV, much bigger than that in conventional semiconductor quantum dots ($\sim$meV). These interactions serve to manipulate spins for possible applications in spintronics and qubits. For sufficiently wide samples, the QBS lifetime can be very long. As a result, charges may accumulate in the QPC and may give rise to dynamical Coulomb blockade effects [49].

The QBS may be visualized using STM, which probes the dressed local density of states (LDOS) directly [50]. One can show that in comparison with the bare LDOS the dressed LDOS is enhanced by an amount $\delta\rho(\varepsilon_F, \vec{r}) \sim \frac{\Gamma_{QBS}}{(\varepsilon-\varepsilon_{QBS})^2 + \Gamma_{QBS}^2} f(\vec{r})$, where $f(\vec{r})$ is a function that decays as the STM tip moves away from a SCB by $|\vec{r}|$, as indicated in Fig. 3(c). The properties of the QBS can thus be directly determined.

The QBS can also have optical signatures. Specifically, we predict the optical absorption to be enhanced at the frequency $\nu \approx \frac{2\varepsilon_\infty}{h}$, which corresponds to the energy required to excite an electron from the lower QBS at $-\varepsilon_\infty$ to the upper one at ε_∞. For

($N_c = 3, m = 2$), this gives $\nu \approx 48$ THz in the infrared regime. Note that the QBS lifetime in this case is $\tau_{\text{QBS}} \approx 7(\frac{N_c}{100})^3$ps, which can be much longer than the optical oscillation period ν^{-1}. Thus, the system may be treated as an artificial two-level atom when dealing with its interaction with light at frequencies near or above ν.

In addition, the QPCs can serve as the channel for a textbook single-level (and single-electron in the presence of Coulomb interactions) resonant tunneling transistor. Due to small level broadening, sharp turn-on can be expected at low temperatures.

VI. CONCLUSION

In conclusion, we elucidated a mechanism for the formation of atomic bound states in a type of graphene QPCs. These states arise because of the zero-energy edge states that are associated with the breaking of pseudo-time-reversal symmetry. Their energies have been shown to be roughly independent of the sample dimensions. Finite level broadening exists, which shrinks to zero following a power law as the sample width increases. Because of the broadening, the states show up as Breit-Wigner resonances in the conductance of the QPCs. Such resonances dominate the electronic transport properties in the low-energy regime.

[1] H. van Houten and C. Beenakker, Phys. Today **49**, 22 (1996).

[2] Y.-H. Zhang, P. Wahl and K. Kern, Nano Lett. **11**, 3838 (2011).

[3] H. van Houten, C. W. J. Beenakker, and B. J. van Wees, Semicond. Semimet. **35**, 9 (1992).

[4] T. Ihn, *Semiconductor Nanostructures: Quantum States and Electronic Transport* (Oxford University Press, New York, 2010).

[5] M. J. Iqbal, R. Levy, E. J. Koop, J. B. Dekker, J. P. de Jong, J. H. M. van der Velde, D. Reuter, A. D. Wieck, R. Aguado, Y. Meir, and C. H. van der Wal, Nature (London) **501**, 79 (2013).

[6] F. Bauer, J. Heyder, E. Schubert, D. Borowsky, D. Taubert, B. Bruognolo, D. Schuh, W. Wegscheider, J. von Delft, and S. Ludwig, Nature (London) **501**, 73 (2013).

[7] I. I. Yakimenko, V. S. Tsykunov, and K.-F. Berggren, J. Phys.: Condens. Matter **25**, 072201 (2013).

[8] Y. Yoon, M.-G. Kang, P. Ivanushkin, L. Mourokh, T. Morimoto, N. Aoki, J. L. Reno, Y. Ochiai, and J. P. Bird, Appl. Phys. Lett. **94**, 213103 (2009).

[9] T. Rejec and Y. Meir, Nature (London) **442**, 900 (2006).

[10] K. Hirose, Y. Meir, and N. S. Wingreen, Phys. Rev. Lett. **90**, 026804 (2003).

[11] K. J. Thomas, J. T. Nicholls, M. Y. Simmons, M. Pepper, D. R. Mace, and D. A. Ritchie, Phys. Rev. Lett. **77**, 135 (1996).

[12] K. J. Thomas, J. T. Nicholls, N. J. Appleyard, M. Y. Simmons, M. Pepper, D. R. Mace, W. R. Tribe, and D. A. Ritchie, Phys. Rev. B **58**, 4846 (1998).

[13] A. K. Geim and K. S. Novoselov, Nat. Mater. **6**, 183 (2007).

[14] D. A. Areshkin and C. T. White, Nano Lett. **7**, 3253 (2007).

[15] L. Tapasztó, G. Dobrik, P. Lambin, and L. P. Biró, Nature Nanotech. **3**, 397 (2008).

[16] A. Girdhar, C. Sathe, K. Schulten, and J.-P. Leburton, PNAS **110**, 16748 (2013).

[17] J. Güttinger, F. Molotor, C. Stampfer, S. Schnex, A. jacobsen, S. Dröscher, T. Ihn, and K. Ensslin, Rep. Prog. Phys. **75**, 126502 (2012).

[18] B. Özyilmaz, P. Jarillo-Herrero, D. Efetov, and P. Kim, Appl. Phys. Lett. **91**, 192107 (2007).

[19] B. Terres, J. Dauber, C. Volk, S. Trellenkamp, U. Wichmann, and C. Stampfer, Appl. Phys. Lett. **98**, 032109 (2011).

[20] M. Y. Han, J. C. Brant, and P. Kim, Phys. Rev. Lett. **104**, 056801 (2010).

[21] C. Stampfer, E. Schurtenberger, F. Molitor, J. Güttinger, T. Ihn, and K. Ensslin, Int. J. Mod. B **23**, 2647 (2009).

[22] P. Darancet, V. Olevano, and D. Mayou, Phys. Rev. Lett. **102**, 136803 (2009).

[23] K. Todd, H.-T. Chou, A. Amasha, and D. Goldhaber-Gordon, Nano Lett. **9**, 416 (2009).

[24] M. Fujita, K. Wakabayashi, K. Nakada, and K. Kusakabe, J. Phys. Soc. Jpn. **65**, 1920 (1996).

[25] K. Nakada, M. Fujita, G. Dresselhaus, and M. S. Dresselhaus, Phys. Rev. B **54**, 17954 (1996).

[26] T. Enoki, Phys. Scr. T **146**, 014008 (2012).

[27] K. Wakabayashi and S. Dutta, Solid State Comm. **152**, 1420 (2012).

[28] H. Karimi and I. Affleck, Phys. Rev. B **86**, 115446 (2012).

[29] A. Rycerz, J. Tworzydlo, and C. W. J. Bennakker, Nat. Phys. **3**, 172 (2007).

[30] K. Wakabayashi, Y. Takane, and M. Sigrist, Phys. Rev. Lett. **99**, 036601 (2007).

[31] D. Gunlycke, J. Li, J. W. Mintmire, and C. T. White, Nano Lett. **10**, 3638 (2010).

[32] J. Guo, D. Gunlycke, and C. T. White, Appl. Phys. Lett. **92**, 163109 (2008).

[33] D. Gunlecke, D. A. Areshkin, J. Li, J. W. Mintmire, and C. T. White, Nano Lett. **7**, 3608 (2007).

[34] K. Wakabayashi and T. Aoki, Int. J. Mod. Phys. B **16**, 4897 (2002).

[35] A. R. Akhmerov, J. H. Bardarson, A. Rycerz, and C. W. J. Beenakker, Phys. Rev. B **77**, 205416 (2008).

[36] H.-Y. Deng, K. Wakabayashi, and C.-H. Lam, J. Phys. Soc. Jpn. **82**, 104707 (2013).

[37] U. Fano, Phys. Rev. **124**, 1866 (1961).

[38] E. N. Economou, *Green's Functions in Quantum Physics* (Springer-Verlag, New York, 1979).

[39] Employing the same approximations, we can derive from Eq. (4) that $T_{i_\tau, i_\tau} \approx -\gamma_0 G_0^{i_{\bar{\tau}}, i_\tau} T_{i_{\bar{\tau}}, i_\tau}$, where $\tau = L, R$ and $\bar{\tau} = R, L$. We note that for energies close to zero $G_0^{i_\tau, i_\tau} \approx 0$ because

of the particle-hole symmetry. Thus, T_{i_τ,i_τ} is much smaller than $T_{i_\tau,i_{\bar\tau}}$.

[40] Contributions from the high-energy sector (consisting of short transverse wavelength modes) are vanishingly small due to particle-hole symmetry. The low-energy section consisting of long-wavelength modes contribute less and less as W increases, since the wave functions scale as $W^{-3/2}$ near edges. Actually, the transverse wave functions of such modes are sine waves (see [27]).

[41] Y. Shimomura, Y. Takane, and K. Wakabayashi, J. Phys. Soc. Jpn. **80**, 054710 (2011).

[42] In Eq. (16), the factor 2 accounts for the fact that of the two degenerate sets of the edge modes obtained in the semi-infinite limit only one contributes near either edge.

[43] We see that Δ decreases with N_z. For our assumption to hold, we must have $\Delta > \varepsilon_\infty \sim 0.01$. Note that $\Delta \approx \frac{20}{2N_z-1}$, from which we infer that the widest possible ribbon should not exceed $N_z \sim$ 1000, i.e., around 150 nm. If N_z indeed exceeds this critical value, one can show that Eq. (18) still holds but the coefficient A has to sum over more channels and subsequently the τ_{QBS} scales as N_z^2 instead of N_z^3 (the additional factor accounts for the number of dispersive bands).

[44] H. A. Bethe, Phys. Rev. **66**, 163 (1944).

[45] J. Bardeen, Phys. Rev. Lett. **6**, 57 (1961).

[46] K. Wakabayashi, Phys. Rev. B **64**, 125428 (2001).

[47] V. P. Gusynin, V. A. Miransky, S. G. Sharapov, I. A. Shovkovy, and C. M. Wyenberg, Phys. Rev. B **79**, 115431 (2009).

[48] T. O. Wehling, E. Sasioglu, C. Friedrich, A. I. Lichtenstein, M. I. Katsnelson, and S. Blügel, Phys. Rev. Lett. **106**, 236805 (2011).

[49] B. R. Bulka, T. Kostyrko, M. Tolea, and I. V. Dinu, J. Phys.: Condens. Matter **19**, 255211 (2007).

[50] J. Tersoff and D. R. Hamann, Phys. Rev. B **31**, 805 (1985).